

**Award Number: G11AP20194 and G11AP20195**

**Improving the Use of Depth Phases in Routine Estimates of Depth  
and Location of Earthquakes: Collaborative Research with  
California State Polytechnic University in Pomona and URS  
Corporation.**

**FINAL TECHNICAL REPORT**

**January 24, 2014**

Hong Kie Thio\* and Jascha Polet<sup>+</sup>

\*URS Group, Inc.  
915 Wilshire Boulevard  
Los Angeles CA 90017

Tel: 213.996.2200  
Fax: 213.996.2290  
Email: hong.kie.thio@urs.com

<sup>+</sup>Department of Geological Sciences  
California State Polytechnic University Pomona  
3801 W. Temple Avenue  
Pomona, CA 91768

Tel: 909-869-3459  
Fax: 909-869-2920  
Email : jpolet@csupomona.edu

Research supported by the U.S. Geological Survey (USGS), Department of the Interior, under award number G11AP20194. The views and conclusions contained in this document are those of the authors and should not be interpreted as necessarily representing the official policies, either expressed or implied, of the U.S. Government.

# **Title:** Improving the Use of Depth Phases in Routine Estimates of Depth and Location of Earthquakes: Collaborative Research with California State Polytechnic University in Pomona and URS Corporation.

## **Authors:**

Jascha Polet  
Department of Geological Sciences  
California State Polytechnic University  
3801 W. Temple Avenue  
Pomona, CA 91768  
Tel.: (909) 869-3459  
Fax: (909) 869-2920  
E-mail: jpolet@csupomona.edu

Hong Kie Thio  
URS Corporation  
915 Wilshire Blvd #700  
Los Angeles, CA 90017  
Tel.: (213) 996-2250  
E-mail: hong.kie.thio@urs.com

## **1 Introduction**

In routine earthquake location algorithms, the hypocenter and origin time are usually obtained by minimizing travel time residuals of seismic phases that represent easily identifiable, isolated arrivals in the waveform, and are well constrained in terms of their arrival time, such as the direct P and S waves. Whereas the horizontal coordinates of earthquake location are generally well-constrained, provided sufficient azimuthal coverage is available, the depth of an event is usually much more poorly determined, and has a significant trade-off with origin time, unless stations are located very close to the source so that observations are available in both vertical directions (up, to the local stations and down, to distant stations). This difficulty in obtaining accurate depths, especially for relatively shallow earthquakes, has led to the common practice of fixing the depths of earthquakes to a specific value, usually 15 or 33 km, to obtain stable results in the location procedure. This problem can be reduced to a large extent if so-called depth phases can be included (Figure 1) in the location inversion, since these phases provide a similar constraint as stations located above an event would give in terms of depth resolution.

We have studied the timing and character of depth phases using 2.5-D travel-time calculations and 3-D finite difference calculations to understand their global variability. Our results indicate that we expect inter-station differences ranging from 5-6 seconds globally, whereas different locations relative to the trench can give rise to differences of up to 10 seconds in differential travel times. A comparison with observed arrival times from the ISC catalog are inconclusive. For our test area, depth phases are primarily reported in a narrow range of azimuths, which may be due to an uneven distribution of land areas and station distributions. The limited azimuthal variation of differential travel times for the depth phases shows an almost random pattern. This may be due to location errors as well as uncertainties in the identification and timing of the picked arrivals.

In order to help in the identification and characterization of depth phases we have also computed 3-D synthetic seismograms for the same area. Due to some unforeseen complications with the stability of the code that required some time to solve, we have carried out the full modeling of the observed seismograms yet, but the preliminary results show that we can model the observed patterns quantitatively.

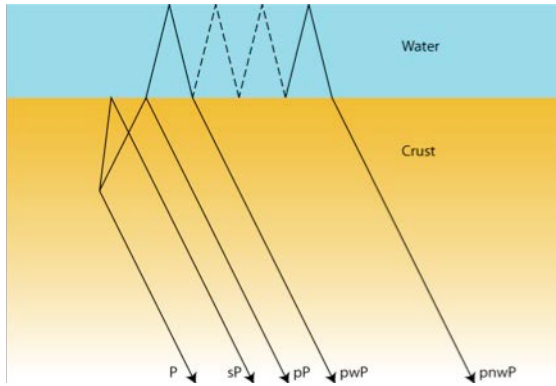


*Figure 1. Cartoon of a 1D velocity model explaining the definition of the pP, sP and pwP rays. Not all possible rays are shown.*

## 2 Methodology

### Travel Time Calculations

We have developed a 2.5D travel times code using a shortest-path type algorithm that efficiently computes the travel times of P or S waves. The method is analogous to the one developed by Podvin and Lecomte (1991) and is highly efficient. We have used this method to compute travel time variations in laterally heterogeneous Earth models for the calibration of travel times to stations of the International Monitoring System (Saikia et al., 2002). A limitation to shortest-path type algorithms is

that they only yield the shortest travel time, i.e. the first arrival of either the P or S wave. In order to compute travel times for depth phases, which are reflected at either the sea surface or the bottom of the sea floor, we have implemented a split approach, where we compute travel times from the source to a reflecting surface, as well as travel times from the station to that surface. This way, we use our shortest path algorithm to compute conditionally shortest travel times, conditional in the sense that the path has to include a reflection on the specified surface.

In order to avoid reflections near the station, and to further improve the efficiency of the method, we limit the calculations of the reflections to a region near the source. The travel times for this region are then interfaced with travel times for the larger model to the station, yielding complete travel times for both the direct wave and the surface and water layer reflected waves. It is also possible to compute converted phases, such as sP, by interfacing the direct S wavefield and coupling it with the surface reflected P wavefield.

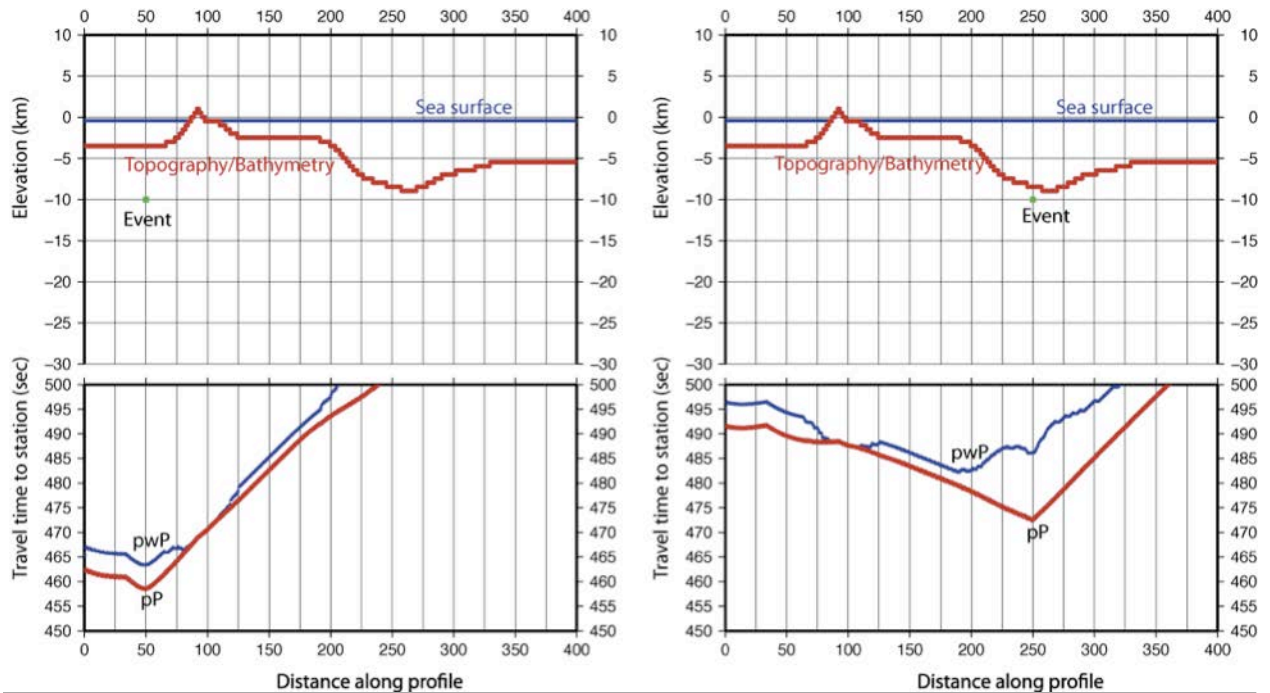


*Figure 2. Example of travel time calculations for depth phases. Source and topography geometry for the Kuril trench are shown in the top panels (based on SRTM30+, Becker et al., 2009), with the total travel times of the reflected rays (pP or pwP) shown below as a function of location along profile of the reflection point. Every point on these surfaces is a potential reflection point, and the actual reflection corresponds to the one with lowest travel time.*

Our method allows for arbitrary velocity structures, and also allows for an irregular (topographic) surface and seafloor. By definition, the 2.5D approach cannot account for off-great-circle propagation of the waves. However, these effects are mostly caused by large-scale anomalies along the longer part of the path and thus likely to be very similar for both the direct P and the reflected sP, pP and pwP phases. If we are primarily interested in the travel time differentials, the 2.5D approach may be a good approximation. For more detailed waveform analysis we can use the 3D finite difference model described in the next section. The advantage to using the 2.5D method in addition to a fully 3D analysis is that it yields actual travel times, whereas in the 3D calculations it is not always straightforward to identify an arrival as pP, sP or pwP. Also, the 2.5D travel time computations are an order of magnitude faster than the 3D models, which allows us to explore a larger set of parameter variations before proceeding with full 3D computations.

In the 2.5D approach, the travel times are computed along a section through the Earth. The model is broken up in two different sections:

1. A teleseismic model, which consists of a coarser grid, where we use the shortest path method to compute travel times from a station to every point in the grid. This model is large enough to allow us to compute direct P waves over their entire distance range (0-100 degrees).
2. A local “box” around the source region, where the travel times are computed using the same method but on a much finer grid. In this box, which is a subregion of the larger teleseismic model, we define the source location and the location of the two main reflectors, the top of the solid Earth and the ocean surface.

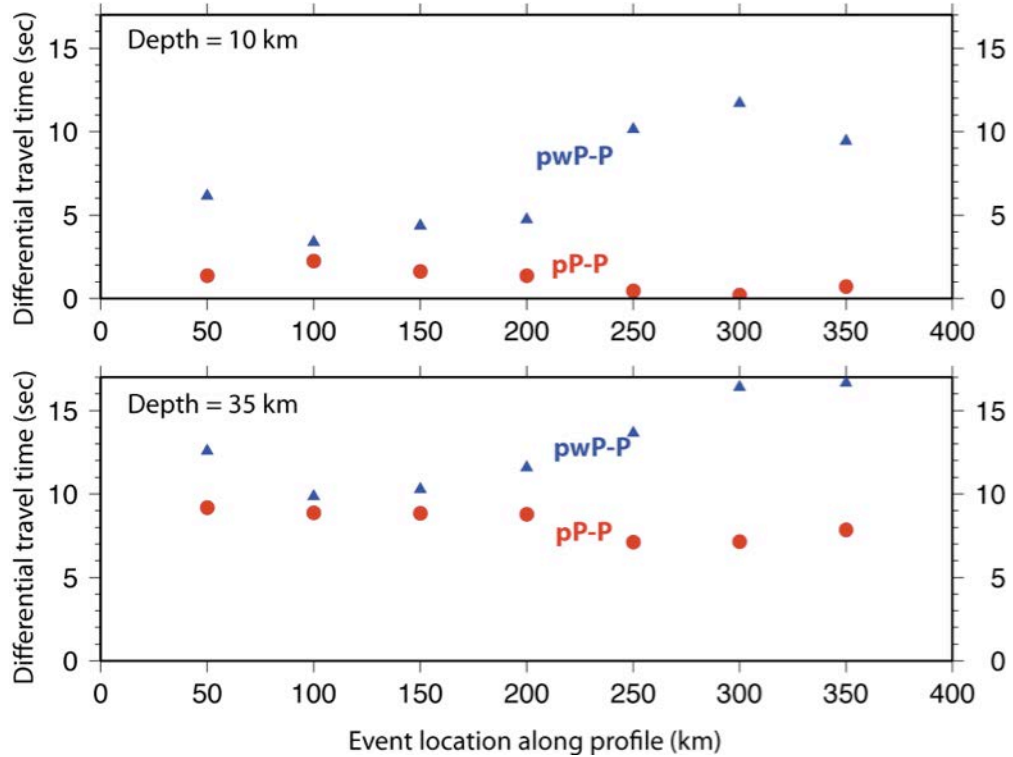


Figure 3. Differential travel times for events located along a profile perpendicular to the Kuril trench. Blue triangles are the  $pwP$  travel times minus the  $P$  travel times ( $pwP-P$ ) and the red triangles are the  $pP$  minus  $P$  travel times ( $pP-P$ ). Note the large variations of up to 7 seconds in the  $pwP$  differentials depending on the source location.

Since we are primarily interested in differential travel times, we use a simple 1D model (ak135) for the teleseismic propagation. We compute the travel times for a whole range of distances, and therefore only need to compute the teleseismic part once. Any source and station pair can be accommodated by choosing the source box within this pre-computed teleseismic model.

In the source box we perform three calculations:

- a forward computation from the source to the edges of the box and the two main reflecting surfaces, i.e. the top of the crust and the top of the water layer,
- a similar calculation but with the  $P$  velocities in the crust replaced by  $S$  velocities, and
- a reciprocal one where we compute the wavefield from the edges of the box to the reflectors using the teleseismic travel times on the edges as starting values.

The latter can be regarded as a continuation of the teleseismic computation but at a much higher resolution. The forward and reciprocal travel times at the reflecting surfaces are then summed, and the travel time for the reflected phases  $pP$  and  $pwP$  for the first and  $sP$  and  $swP$  for the second set of calculations from a chosen source to a chosen receiver are the minimum travel times of their associated reflecting surfaces. The direct  $P$  travel time is found by simply picking the travel time at the source point for the reciprocal calculations. This calculation can be extended to include multiple bounces by computing the travel-times from every point on the seafloor to every point on the surface, but we have currently limited ourselves to the first reflections.

As an example we computed the differential travel times for several sources on both sides of the Kuril trench (Figure 2). In this case we only considered the effect of the topography on the

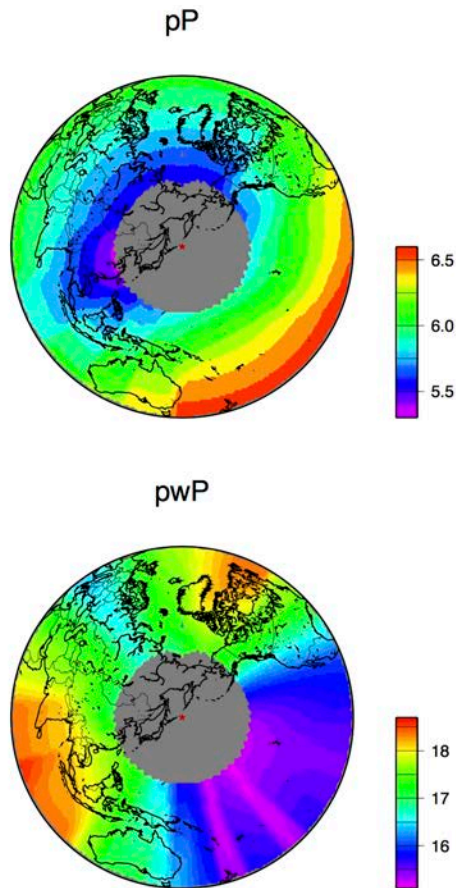


Figure 4. Global distribution of travel-time differentials for pP and swP for an event in the Kuriles.

depth phases and used a 1D velocity model. In the top panels of Figure 2 we show the topography and sea surface as well as the source location for two examples. In the lower panels, the graphs show the total travel time from the source to the station with the condition that the path includes a reflection from either the ocean surface (blue) or from the top of the solid Earth (red). These times are simply the sum of the reciprocal (station to reflector) and the forward (source to reflector) calculations. The minimum of those travel time curves corresponds to the actual reflected wave, and the location of the minimum is where the bounce point is located. In the relatively simple left hand side of the model, the corresponding reflections are also relatively simple with the bounce points almost directly above the event. In the more complicated situation near the trench, on the right, the bounce point for the pP wave is almost right on top of the event, which is expected since it is located very close to the top of the crust, but the pwP bounce point appears to be located almost 50 km to the left. This strong asymmetry also means that we can expect the differential travel times to be highly dependent on the azimuth to the station.

In Figure 3 we show the computed differential travel times for two sets of events at different depths (10 and 35 km) distributed perpendicular to the trench. It is clear that there is a very large range of differential travel times for events, depending on their location along the profile.

### 3D Finite Difference Wave Propagation Technique

Studies of wave propagation based on three-dimensional finite-difference methods (3D-FDM) have contributed to a better understanding of the heterogeneous path and source process. A common feature of the 3D-FDM techniques used in modeling wave propagation is the use of the uniform-grid formulation with constant grid spacing, which requires relatively large computer memory.

Due to computational limitations, the wave propagation modeling is consequently restricted to long periods (usually longer than 1 sec). 3D-FDM techniques capable of extending these calculations to shorter period seismograms at large distances without requiring additional computer memory are essential to understand the influence of the propagation model in the regions where geologic features are complex. A significant improvement in the 3D-FDM technique was made by the application of the finite-difference operators on 3D grids with variable spacing (Pitarka, 1999). This, combined with parallel processing, enables the modeling of wave propagation at high frequencies using realistic velocity models (Cotton et al., 1998; Sekiguchi

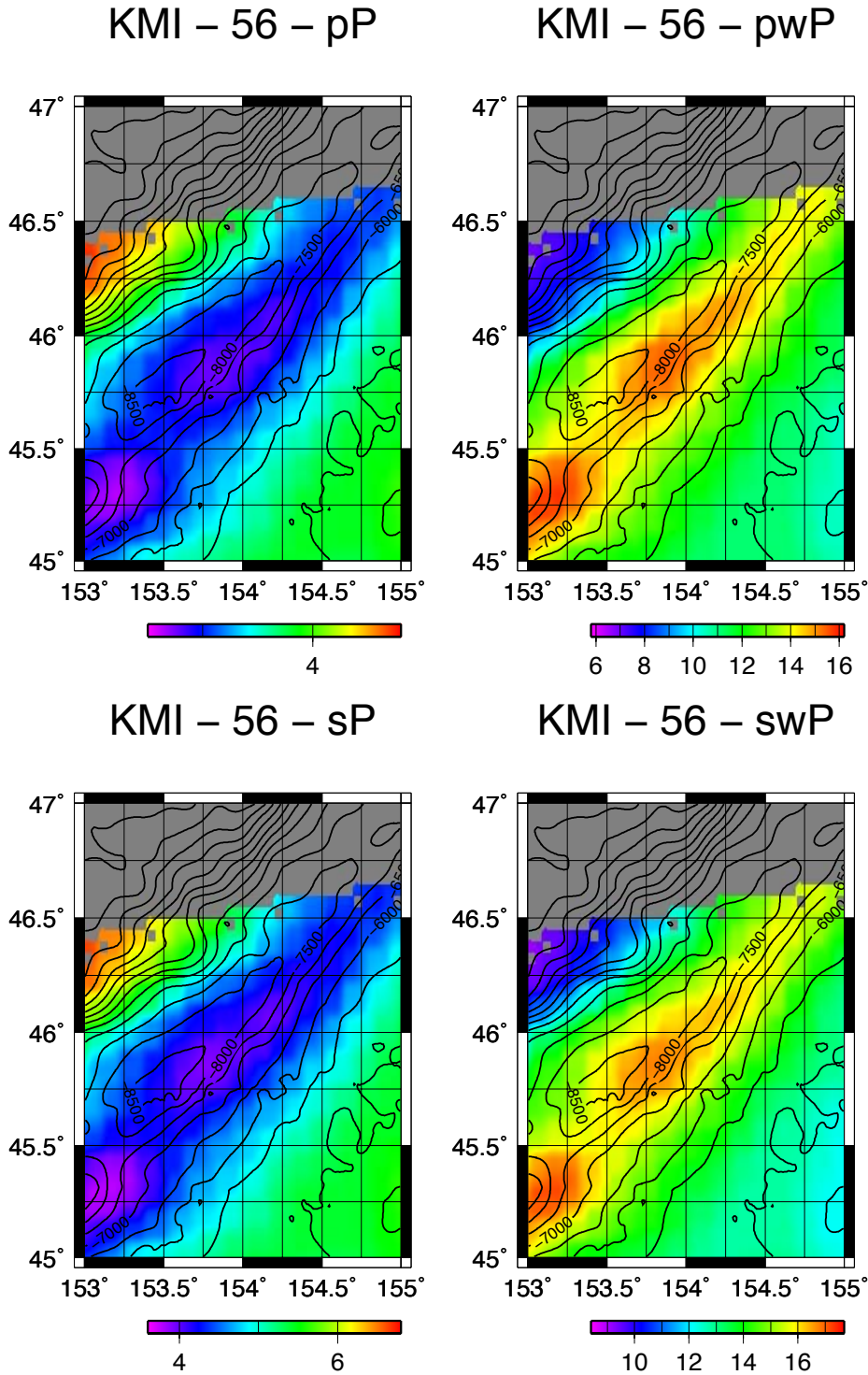


Figure 5. Travel time differentials for event locations around the Kurile trench. Event depth is 18 km.  
 and Iwata, 2000). Our 3D-FDM computer code solves the stress-velocity equations in a

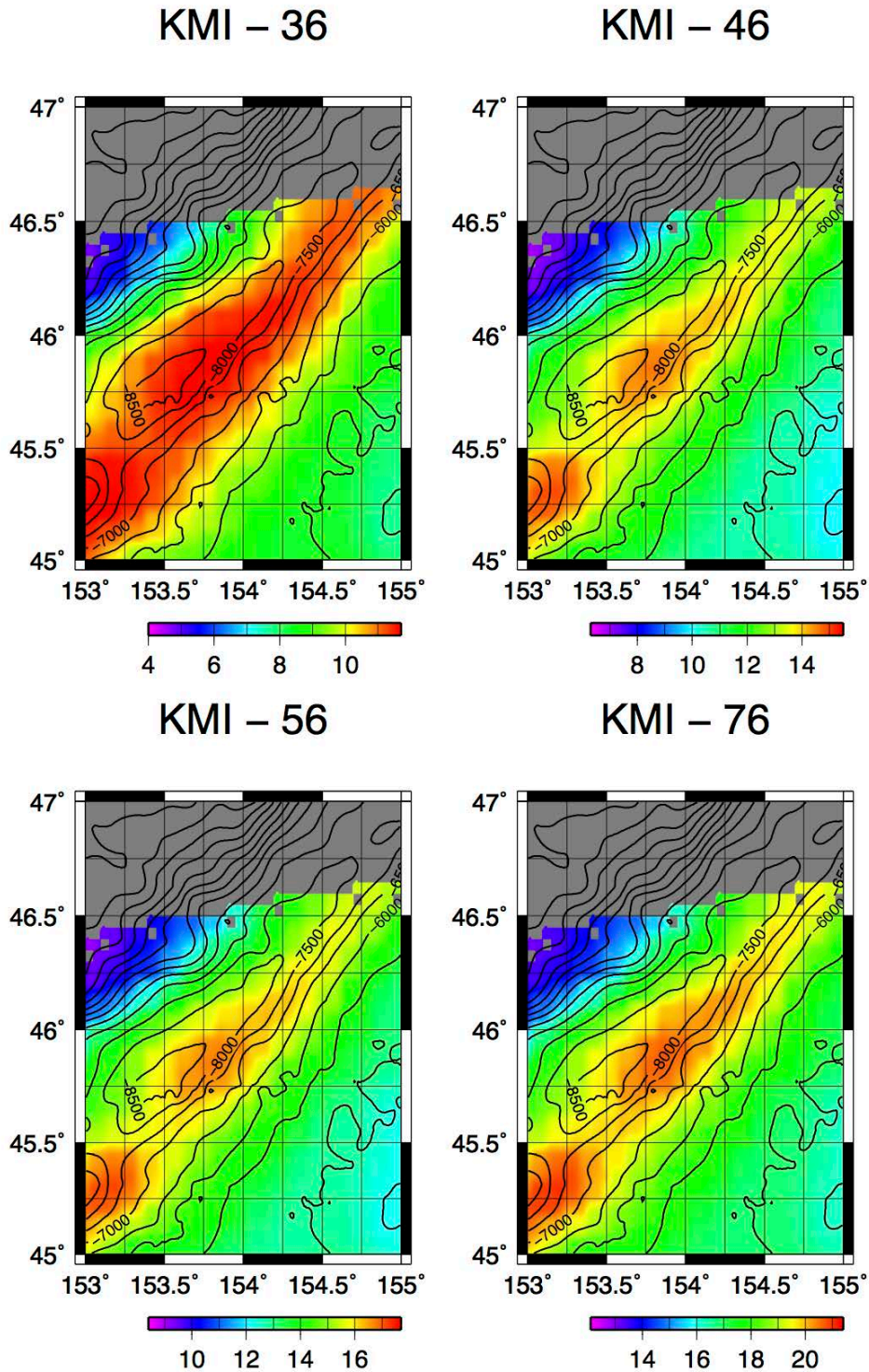


Figure 6. Travel time differentials for P-swP for a range of depth (8, 13, 18 and 28 km respectively).

heterogeneous medium using staggered grids based on such technique. The code can also treat heterogeneous structure with surface topography (Pitarka and Irikura, 1996), in addition to wave propagation in water. Anelastic attenuation is implemented efficiently using relaxation times between stress and strain based on the viscoelastic modulus representation (e.g., Graves and Day,

2003). The performance of our free-surface boundary condition technique has been validated against other standard and accurate techniques for modeling surface topography such as the 2D-Boundary Element Method (BEM) and the 2D-Discrete Wavenumber-Boundary Integral Equation method of Takenaka et al. (1996). Major recent improvements to the software include the interfacing between local finite difference results with teleseismic rays, which allows us to efficiently compute the teleseismic signal from a complex 3D source region.

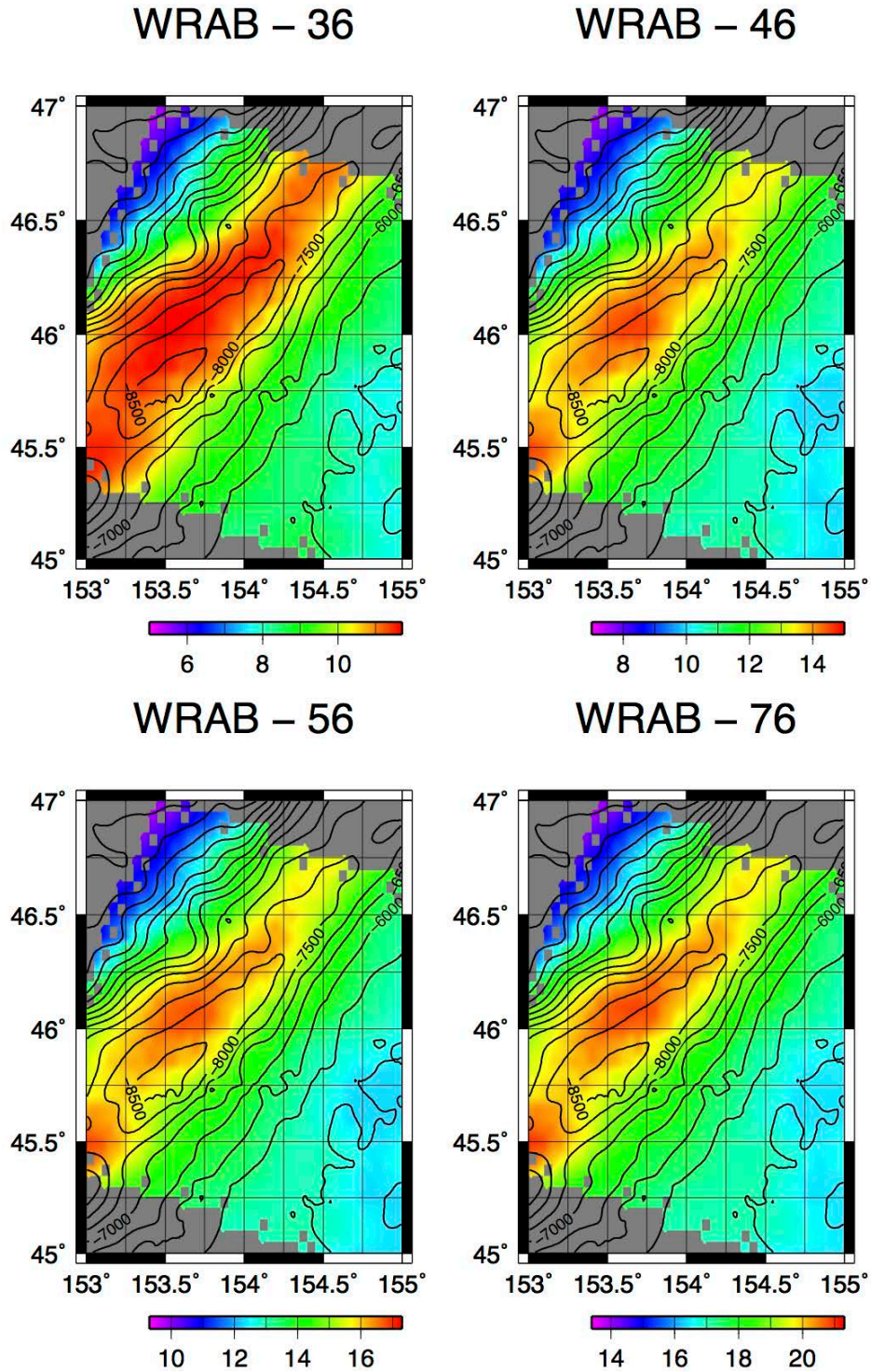


Figure 7. Same as Figure 6 for station WRAB.

### Interfacing 3D Numerical Solver With Ray Theory

In this study we propose to model tele-seismic P waves by interfacing near-field point source seismograms computed using a parallelized staggered grid finite-difference (FD)

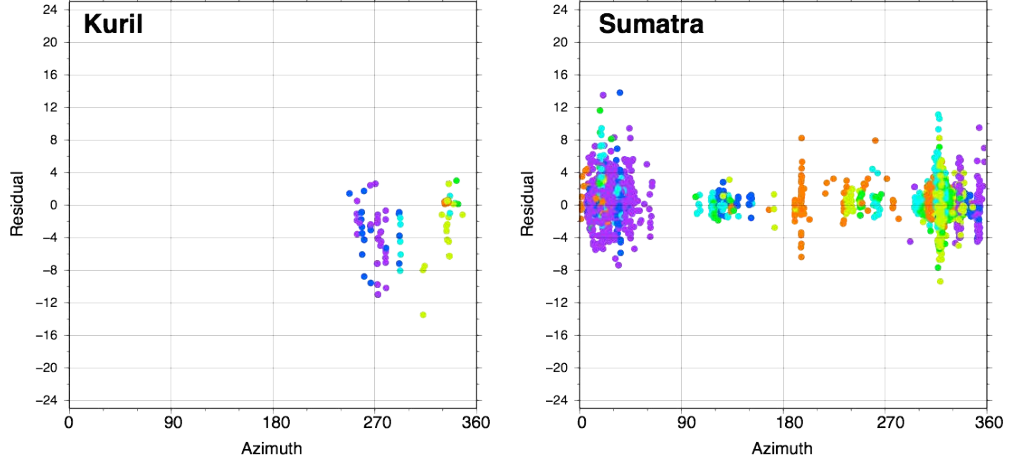


Figure 8. Azimuthal distribution of observed differential ( $P$ - $pP$ ) travel time residuals for events in our test area (left). Because of the large azimuthal gap in station coverage we also show data for events in the Aceh subduction zone which has a more uniform coverage.

algorithm (Pitarka, 2007) for a local 3D Earth model with the 1D tele-seismic seismograms calculated using ray theory. Our approach is similar to the interfacing technique proposed by Saikia et al. (2007). To propagate the near-source wave field to a tele-seismic distance, the point-source FD wave-field is first stored on five planes surrounding the local 3D structure, including a horizontal plane at a specific depth below the source, and four vertical planes bounding the structure (Figure 6). In a second step this wave-field is propagated to tele-seismic distances using the following scheme.

From ray theory the displacement function for a tele-seismic P wave is:

Following Aki and Richards (2.41) and using integration by parts we obtain:

$$u_n(x,t) = \int d\tau \iint \left[ u_i(\xi, \tau) C_{ijpq} \gamma_j \frac{\partial G_{np}}{\partial q} - G_{np}(x, t - \tau, \xi, 0) S_p(u(\xi, \tau), \gamma) \right] d\Sigma$$

where  $K$  is the departure vector,  $F$  the source time function, and  $N$  is the normal vector to the

$$u_n(x,t) = \iiint \left\{ v(\tau) \left[ \frac{\lambda N + 2\mu K(NK)}{\alpha(\xi)} \right] + KS(\tau)N \right\} A(x) Amp(x, \xi) F(t - \tau - T(x, \xi)) d\Sigma d\tau$$

interface. The particle velocity  $v$  and stress  $S$  on the interface are calculated using a 3D finite difference method. The summation of individual contributions over the planar interface  $\Sigma$  will give the tele-seismic displacement  $u_n(x,t)$ . This scheme is very fast and easy to implement into a 3D computer code.

## 3 Implementation and results

### 3.1 Ray tracer

#### 3.1.1 Computations

All the travel-time results were computed on a 2.66 GHz Intel Core 2 MacBook Pro with 4GB of RAM. The test area was sampled with grid sizes of 0.5 km. As mentioned, the

computations are carried out in three steps: the computation times for a single local slice take 5-10 seconds.

### 3.2 Test area

We applied the aforementioned methods using the 2006 Kuril earthquake as test bed. A complete three-dimensional velocity model for the Kuril trench region was determined from reflection seismology ([http://www.jamstec.go.jp/jamstec-e/IFREE\\_center/data-e/cruise\\_data-e/KY00-05vmodel-e.html#hk101](http://www.jamstec.go.jp/jamstec-e/IFREE_center/data-e/cruise_data-e/KY00-05vmodel-e.html#hk101)). Along the northern Kuril trench, a great ( $M_w=8.3$ ) earthquake occurred on the shallow interface between subducting and overriding plate on November 15<sup>th</sup>, 2006 (Figure 7). This event was followed on January 13<sup>th</sup> of 2007 by the largest ( $M_w=8.1$ ) outer-rise normal fault event ever recorded by a modern global seismic network. The epicenters of these two major earthquakes are separated by less than 100 km in distance. One year after the latter of these two events another, deeper, thrust event occurred, smaller in magnitude ( $M_w=7.4$ ), with a source mechanism and location that suggests it occurred within the subducting plate. The epicenter of this third earthquake was located slightly northwards, but still within 100 km of the epicenters of both previous events. Finally, another, smaller, event occurred April 7<sup>th</sup> 2009.

The numerous aftershocks of these earthquakes of the past 4 years, located in close proximity of each other, but diverse in terms of source mechanism, depth and horizontal location relative to the trench, offer a unique opportunity in the study of the importance of the incorporation of three-dimensional subduction zone structure on depth phases. Due to their proximity, any relative path effects due to velocity anomalies away from the immediate source region are minimized. However, a strong azimuthal variation in the tele-seismic P-waveforms may be expected, due to the diversity of the structure “seen” by the rays as they leave the source. The details of the waveforms will depend on the behavior of the direct P-wave that leaves the source in a downwards direction, in combination with the depth phases, which will leave the source upwards and reflect off discontinuities above the source, such as the ocean floor, the ocean-air interface, or the dipping slab interface.

### 3.3 2.5-D Travel times

We implemented the 2.5-D ray tracer to the subduction zone environment with realistic velocity structure, topography and bathymetry. We have concentrated on the main depth phases of pP, pwP, sP and swP.

### 3.4 Global patterns of travel-time differentials

In Figure 4, we present a map of global travel time residuals for P-pP, p-pwP, and P-sP for an event in the test area. The variations of the travel-time residuals are on the order of 4 seconds for pwP and only 1 second for pP. This is due to the fact that the differences for the pP paths in different azimuths are much smaller than those of the pwP paths. The largest differential travel times for the pwP phase are clearly in the direction of the trench axis, which is to be expected since these paths encounter the thickest average water column. The pP reflection on the other hand show smaller differentials in this direction, since the path for these rays is shorter due to the thinner crust.

### 3.5 Travel-times and location relative to the trench

Although the previous map is very illustrative to understand the effect of local structure on the global distribution of travel-time differentials, for location purposes it is more useful to see how the differentials vary as a function of source locations. In Figure 5 we present maps for the differential travel times (P-pP, P-pwP, P-sP, P-swP) from the test area to a single station for different event locations. The range of differential times between different event locations is much larger than the inter-station variability for a single event. Especially the water phases are sensitive to changes in the bathymetry.

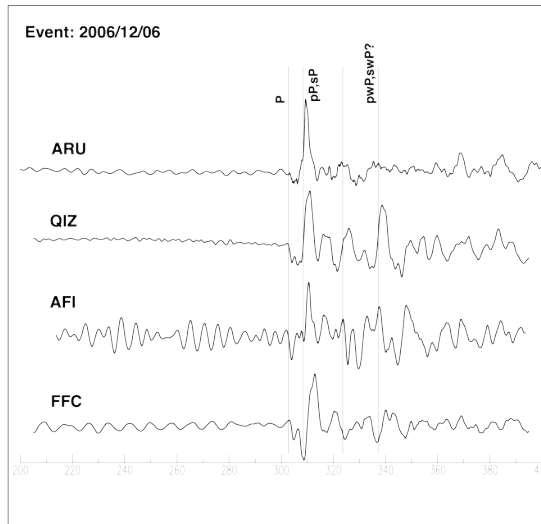


Figure 9. Observed broadband seismograms for the 2006/12/07 Kuril earthquake in trench parallel directions (QIZ and FFC) as well as landward direction (ARU) and seaward direction (AFI).

phases and when plotted against azimuth (Figure 8), there is no clear pattern discernible for our test area. This is partly due to the narrow azimuthal range of the data, as most of the depth phase observations come from Chinese stations, but is also due to the large scatter. Unfortunately, it's difficult to establish whether this scatter is due to difficulty in timing, mis-identification of phases, or whether it reflects a real property of the Earth's structure. When looking at data from the Aceh subduction zone however, there appears to be much larger scatter to the North and South, which is roughly in the trench parallel direction. This suggests that either there is very strong variability of depth phases in that direction, or that the depth phases (primarily pP) are more ambiguous and easily misidentified.

Several seismograms for an event in the area ( $M_w=6.4$ ) shown in Figure 9 exhibit significant ringing after the first wave arrival. However it is difficult to identify individual phases and we will explore this issue by using 3-D synthetic seismograms.

### 3.7 3-D waveform modeling

We encountered some unexpected complications during the implementation of the 3-D code, some of which were only resolved recently. A major issue turned out to be leakage from the S wave-field into the tele-seismic P-waves. Ultimately, this issue was resolved by applying a very low S velocity in the bottom of the crust which, due to the steep take-off angle of the tele-seismic P-waves, has no significant effect on those rays. The computations were carried out on a 24 and 32 CPU parallel processor. With a cell-size of 250 m and dimensions of 200x200x100 km the runs usually last between one and two hours.

We show 3D waveform synthetics computed for a simplified version of this model in Figure 10. Effects of the pronounced structural complexities, such as large later arrivals, are in many cases not reproduced by a one-dimensional flat-layered velocity structure. These synthetics were computed for a model that is very similar to the one used for the travel-times calculations. The effect of the water layer and dipping structure is particularly evident for the shallower event by comparing the NW and SE directions. The locations of the source have been indicated on the velocity and topographic profile on top. We intend to use this model in the near future to study

Comparing the results for two different stations at different azimuths, KMI (Figure 6) to the west and WRAB (Figure 7) to the south, we find that although the differentials are on the same order, the peak differentials are shifted to either side of the trench, with the largest anomalies on the opposing side from the direction to the station. Those rays sample the deepest part of the ocean and thus have longer travel times. If depth phases can be identified reliably, this would allow us to locate earthquakes more accurately in areas with large topographical variations. The depth dependence of the differentials is shown in Figure 6,7. It is clear that the variability diminishes as the hypocenter depth increases and become more concentrated near the trench.

### 3.6 Observations

We have collected some depth phase data for our study area from the ISC Bulletin.

Overall, there are not many reports for depth

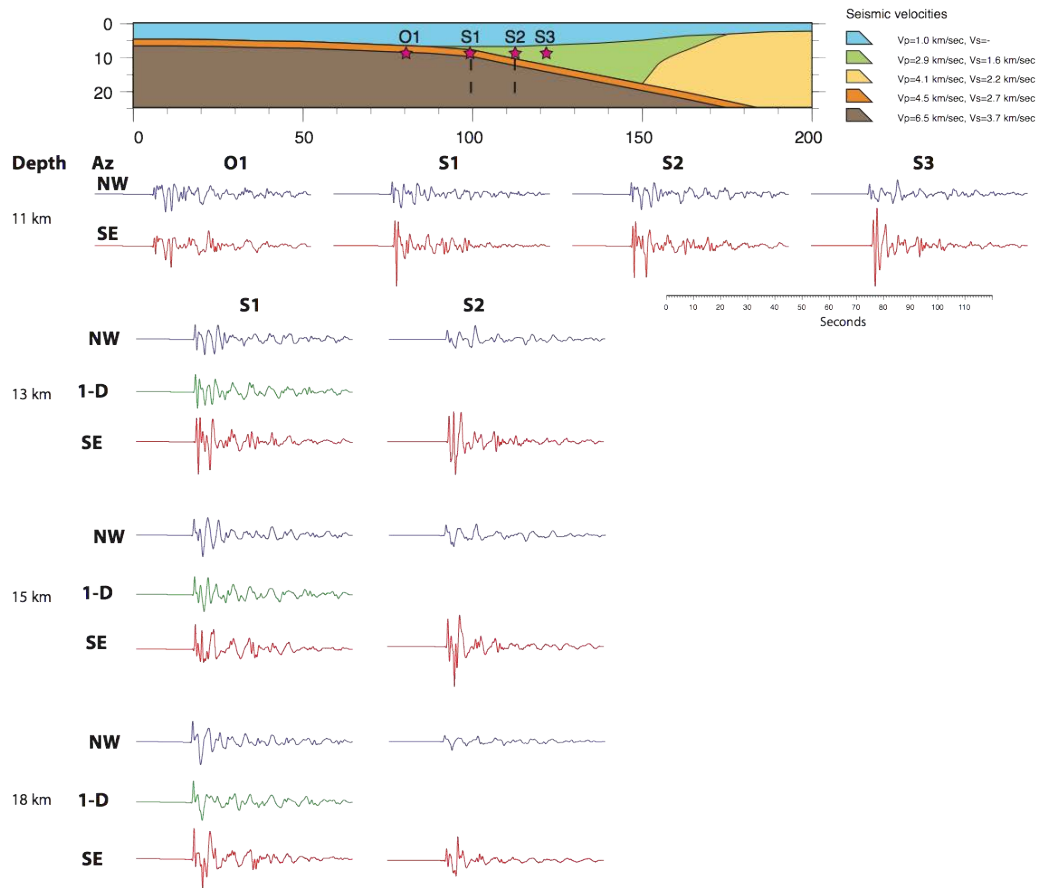


Figure 10. 3D waveforms for earthquakes in the Kuril area at teleseismic distances and different depths.

records such as shown in Figure 9, which in combination with the travel time study, will help us understand those results and lead to an improved practice of identifying and using depth phases for earthquake locations.

An example of a more systematic survey of the spatial variability of depth phases is shown in Figures 11 and 12. In the former, we show three suites of teleseismic seismograms for depths ranging from 7 to 13 km in three different locations, at the outer-rise (A), at the trench (D) and on the landward side (G). In each case, the move-out of the pP and sP phases relative to the direct P are clearly visible, although there are some subtle differences between the different locations. The differences for the water bounces are more distinct, with D and G showing multiple bounces for the pwP phase, which is most likely due to the dipping structures. As the depth increases though, these differences become smaller, and the water bounces themselves are significantly reduced in amplitude.

Looking at the azimuthal variation of depth amplitudes (in particular pwP and swP) (Figure 12) we observe that these tend to be stronger developed in the 180-150 degree azimuth (in the backarc direction) than in other directions. This is observed consistently for different focal mechanisms and suggests that this quadrant is more likely to yield usable water bounces than other directions, and is probably due to the simpler structure and deeper average water depths on the back-arc side than in the landward direction. There is also a clear move-out of the pwP/swP phases from the landward-side towards the trench, which is consistent with our results from the

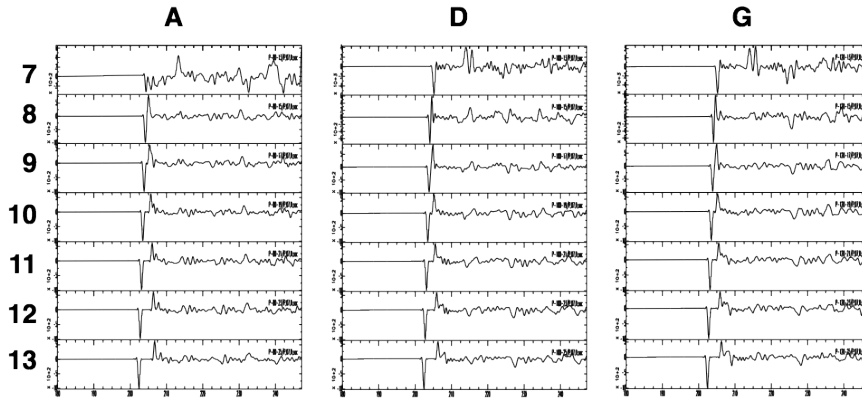


Figure 11. Depth sections for three locations across the trench. The move-out of the pP and sP phases is clearly visible. The pwP phases are visible later in the records.

travel-time calculations (Figure 7). Beyond the trench, these phases are not as clearly defined. For the pP/sP waves, we do not observe any significant azimuthal differences in complexity or timing that might explain the azimuthal pattern seen in the Aceh residuals.

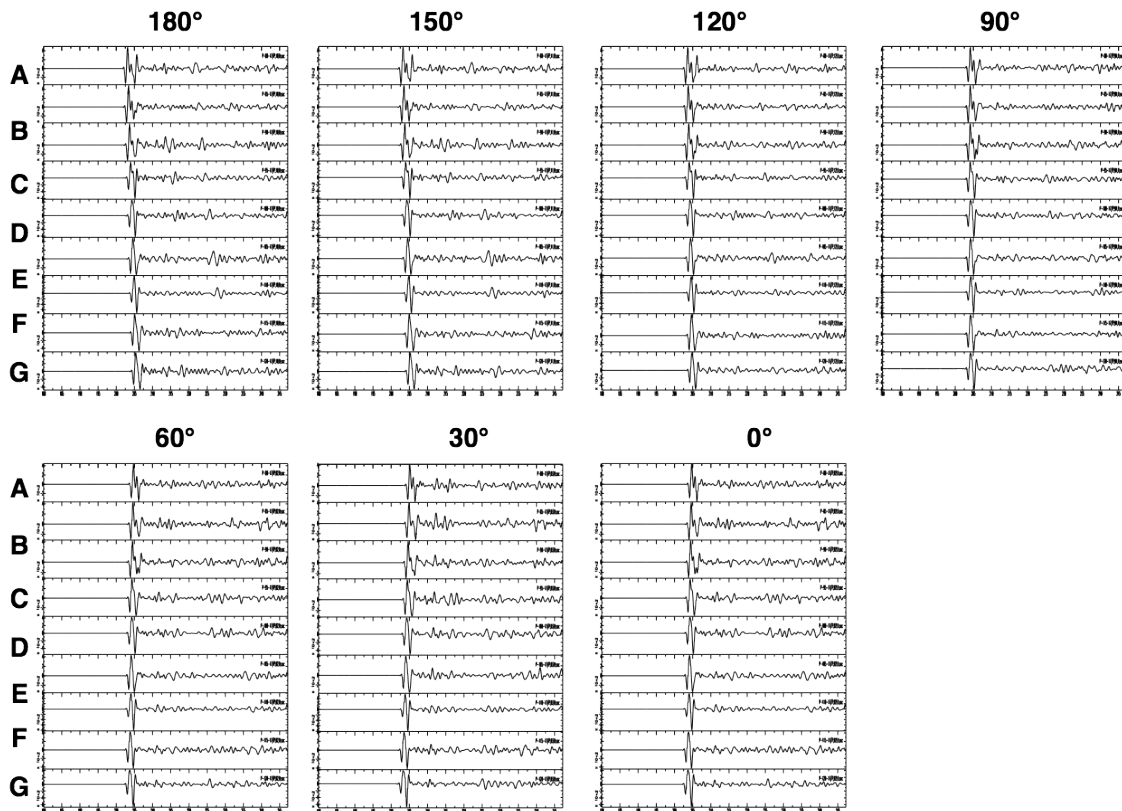


Figure 12. Records for source location across the trench (5 km apart with the trench at location D) (Depth = 8 km), at different azimuths. The strike of the subduction zone is 270 degrees.

## 4 Conclusion

We have shown that there are significant azimuthal variations in differential travel-times for events that occur near the trench. These differentials are most pronounced in the water bounces pwP and swP. These various depth phases may be difficult to distinguish in actual data, but especially for the shallower events, the pP and sP pair, and pwP and swP pair are well separated from each other so that they can still contribute to a better depth estimate even if we are not sure which exact phase (e.g. pP or sP) is observed. The large variations in differential travel times due to the topography/bathymetry suggests that these phases may help to not just constrain the depth but also the event location within the trench region.

A comparison with observed travel time differentials (pP-P) does not yield conclusive results. Although we see some azimuthal pattern for the Aceh subduction zone, there is no clear pattern apparent in the synthetic seismograms. This may be due to misidentification of phases, and the inherent uncertainty in picking the arrival of a secondary phase. The added complexity of the water reverberations may make the identification even more difficult than usual. Our preliminary 3-D modeling results suggest that this technique may help us identify the water bounce depth phases in the future as they seem to be consistently stronger in the back-arc direction than in other directions. Our travel-time code may be useful in evaluating these phases and use them in earthquake locations.

## 5 References

- Becker, J. J., D. T. Sandwell, W. H. F. Smith, J. Braud, B. Binder, J. Depner, D. Fabre, J. Factor, S. Ingalls, S-H. Kim, R. Ladner, K. Marks, S. Nelson, A. Pharaoh, R. Trimmer, J. Von Rosenberg, G. Wallace, P. Weatherall, 2009. Global Bathymetry and Elevation Data at 30 Arc Seconds Resolution: SRTM30\_PLUS, *Marine Geodesy*, 32:4, 355-371.
- Benz, H., Buland, R., Johnson, C., Bittenbinder, A. and S. Sipkin, 2005. HYDRA: NEIC's New Real-time Earthquake Response System. SSA 2005 Annual Meeting, Lake Tahoe, April 27-29.
- Bowers, 2001. Interpretation of P seismograms from shallow undersea earthquakes, *Bulletin of the Seismological Society of America* vol. 91 (3) pp. 628-631.
- Cotton, F., C. Berge, F. Lemeille, A. Pitarka, M. Lebrun, M. Vallon, 1998. Three dimensional simulation of earthquakes in the Grenoble basin, in "The effects of surface geology on seismic motion", Irikura, Kudo, Okada, Sasatani, eds., Balkema, Rotterdam.
- Earle, P.S., and Wald, D.J., 2007, PAGER—Rapid assessment of an earthquake's impact: U.S. Geological Survey Fact Sheet 2007-3101, 4 p.
- Engdahl, E.R., R. vd. Hilst and R. Buland, 1998. Global teleseismic earthquake relocation with improved travel times and procedures for depth determination, *Bull. Seismol. Soc. Am.*, 88, 722-743.
- Engdahl, E.R., and A. Villaseñor, 2002. Global seismicity, in *International Handbook of Earthquake and Engineering Seismology*, Lee, Kanamori, Jennings and Kisslinger, eds., 665-690.
- Engdahl and Billington, 1986. Focal depth determination of central Aleutian earthquakes. *Bulletin of the Seismological Society of America*, vol. 76 (1) pp. 77-93.
- Graves, R. and S. Day, Stability and accuracy of the coarse-grain viscoelastic simulation, *Bull. Seismol. Soc. Am.*, 93, 283-300, 2003.
- Hayes, G, 2009. Subduction zone geometry, Preliminary Result of the 2009/04/07 Kuril Islands Earthquake, [http://earthquake.usgs.gov/eqcenter/eqarchives/subduction\\_zone/us2009fdak](http://earthquake.usgs.gov/eqcenter/eqarchives/subduction_zone/us2009fdak)
- Okamoto, T. and T. Miyatake, 1989. Effects of near source seafloor topography on long-period teleseismic waveforms, *Geophys. Res. Lett.*, 16, 1309-1312.

- Pitarka, A. and K. Irikura, 1996. Modeling 3D surface topography by finite-difference method: Kobe-JMA station site, Japan, case study, *Geophys. Res. Lett.*, 23, 2729-2732.
- Pitarka, A., 1999. 3D Elastic finite-difference modeling of seismic motion using staggered grids with nonuniform spacing, *Bulletin of the Seismological Society of America*, 89, 54 - 68.
- Podvin, P., and Lecomte, I., 1991. Finite difference computation of travel times in very contrasted velocity models: a massively parallel approach and its associated tools, *Geophys. J. Int.*, 105, 271-284.
- Saikia, C. K., A. Pitarka, and G. Ichinose, Propagation of the Near-Field Point Source Finite-Difference Seismograms to Teleseismic Distances Using Propagator Matrices. SSA 2007 Annual Meeting, Abstracts, 2007.
- Saikia, C. K., L. Zhu, B. B. Woods and H. K. Thio (1999). Path calibration and source characterization in and around India, 21st Seismic Research Symposium: Tech. For Monit. CTBT, 243-253.
- Saikia, S.K., H.K. Thio, G. Ichinose and B.B. Woods, 2002. Regional wave propagation and influence of model-based and empirical SSSCS on locations in and around the indian subcontinent, Proceedings of the 24th Seismic Research Review, Ponte Vedra Beach, Florida, 412-419.
- Sekiguchi, H. and T. Iwata, 2000. Fault geometry at the rupture termination of the 1995 Hyogoken Nanbu earthquake, *Bull. Seismol. Soc. Am.*, 90 , 117-133.
- Takenaka, H., B. L. Kennett, and H. Fujiwara. Effect of 2-D topography and 3-D seismic wave field using a 2.5-D discrete wavenumber-boundary integral equation method, *Geophys. J. Int.*, 124, 741-755, 1996.
- Wiens, D., 1989. Bathymetric effects on body waveforms from shallow subduction zone earthquakes and application to seismic processes in the Kurile trench, *J. Geophys. Res.*, 94, 2955-2972.